Materials Research. 2025; 28(suppl. 1): e20250098
DOI: https://doi.org/10.1590/1980-5373-MR-2025-0098

Enhancing Hydrogen Production from Sodium Borohydride: Optimizing MIL-100(Fe) Synthesis for Superior Catalytic Performance

W. E. S. Vieira[a], *E. S. Souza*[a], *J. E. K. Barros*[b], *B. S. Barros*[c]*

[a]*Universidade Federal de Pernambuco, Centro de Ciências Exatas e da Natureza (CCEN), Programa de Pós-Graduação em Química, Av. Jornalista Aníbal Fernandes, s/nº, Cidade Universitária, 50740-560, Recife, PE, Brasil.*
[b]*Universidade Federal de Pernambuco, Centro de Ciências Exatas e da Natureza (CCEN), Departamento de Química Fundamental, Av. Prof. Morais Rego, 1235, Cidade Universitária, 50670-901, Recife, PE, Brasil.*
[c]*Universidade Federal de Pernambuco, Centro de Tecnologia e Geociências (CTG), Departamento de Engenharia Mecânica, Av. da Arquitetura, s/nº, Cidade Universitária, 50740-550, Recife, PE, Brasil.*

Received: January 11, 2025; Revised: June 06, 2025; Accepted: July 13, 2025

The MOF MIL-100(Fe) was successfully synthesized using both a conventional solvothermal method and an innovative green synthesis approach. It was characterized using FTIR, PXRD, TG-DTA, BET, and SEM techniques, and tested for hydrogen production through the hydrolysis of sodium borohydride ($NaBH_4$). The catalyst produced through a green synthesis approach demonstrated superior catalytic performance, achieving a hydrogen generation rate of 443.46 mL min^{-1} g_{cat}^{-1} at 340.15 K, with an activation energy of 16.2 kJ mol^{-1}, and good recyclability over multiple cycles. This is attributed to its higher specific surface area (1224 m^2/g) and greater porosity than the solvothermal synthesized material, which presented a higher activation energy (19.0 kJ mol^{-1}). These findings position MIL-100(Fe) synthesized via green methods as a promising candidate for sustainable hydrogen production.

Keywords: *Catalysis, hydrogen, MIL-100(Fe), green synthesis, sodium borohydride.*

1. Introduction

Global economic growth, population increases, and technological advancements are driving the rising demand for primary energy sources such as oil, coal, and natural gas, which together account for around 85% of global energy consumption. This high level of consumption leads to the emission of approximately 36 billion tonnes of CO_2 each year[1-3]. There is, therefore, consensus on the need for policies to mitigate greenhouse gas emissions (GEE). To achieve this goal, strategies include the use of renewable energies such as solar, wind, and biomass. Additionally, CO_2 capture and utilization technologies, along with energy carriers and clean fuels such as hydrogen (H_2), have been considered[4].

Hydrogen production has become increasingly important in the global energy transition due to its versatility. As a clean energy source, hydrogen plays a crucial role in reducing carbon emissions. Additionally, it offers advantages such as high energy density and widespread availability. Its thermal power is 140.4 MJ/kg, which is 3 to 4 times greater than that of hydrocarbon fuels such as coconut oil and gasoline[4-6].

Hydrogen gas is a lightweight molecule with a very low density. For instance, 1 kg of $H_2(g)$ occupies over 11 m^3 at room temperature and atmospheric pressure, which presents storage challenges. To effectively store hydrogen, pressures between 20 and 70 MPa are required, depending on the type of pressure vessel utilized. Additionally, cooling hydrogen to a temperature of 38 K is also necessary for certain storage techniques[7]. Thus, there is a significant investment in Hydrogen Carriers as a technology for H_2 storage. These compounds can store H_2 molecules through catalytic hydrogenation and release them via catalytic dehydrogenation reactions[4].

Boron-based materials, such as borohydrides ($LiBH_4$ and $NaBH_4$) and ammonia borane (NH_3BH_3), are promising carriers for hydrogen storage due to their high gravimetric storage capacities[8]. Sodium borohydride ($NaBH_4$) is notable for its high hydrogen content (10.7 wt %), safety, water stability, non-flammability, and its capacity to generate hydrogen through hydrolysis reactions, making it ideal for storage. The hydrolysis of $NaBH_4$ is a catalytic process that theoretically produces four moles of $H_2(g)$ for each mole of $NaBH_4$, as shown in the chemical Equation 1 below[9,10]:

$$NaBH_{4(aq)} + 4H_2O_{(l)} \rightarrow NaB(HO)_{4(s)} + 4H_{2(g)} \quad (1)$$

By conducting the reaction of $NaBH_4$ with its deuterate analog $NaBD_4$, using mixtures of H_2O, D_2O, and H_2O/D_2O, Guella et al.[11] indicated that half of the hydrogen produced comes from the BH_4^- anions and the other half from water, proven by the presence of deuterium atoms in the product. During hydrolysis, only hydrogen is released as a gas, which excludes the need for final purification of the material. This exothermic and spontaneous reaction still produces as a by-

*e-mail: braulio.barros@ufpe.br
Associate Editor: Eliana Muccillo.
Editor-in-Chief: Luiz Antonio Pessan.

product the non-toxic sodium metabolite that can be recycled to form the corresponding borohydride.

Due to the slow reaction speed of $NaBH_4$ hydrolysis for hydrogen production at room temperature, a suitable catalyst is typically used to accelerate the reaction. Catalysts of precious metals have been widely discussed due to their stable chemical properties and good catalytic activity, such as Pt[12], Pd, and Ru[13]. However, the high cost and limited availability limit its widespread application. Therefore, developing an active, durable, and low-cost catalyst for the hydrolysis reaction of $NaBH_4$ is the key to the efficient production of hydrogen[14].

Materials based on non-precious metals are also a desirable alternative, among which the cobalt, iron, and nickel catalysts stand out. For example, Lin et al.[15] synthesized carbon-supported Co catalysts and obtained an HGR value (hydrogen generation rate) in the $NaBH_4$ hydrolysis reaction of 4.9 L_{H2} min^{-1} g_{cat}^{-1} to 303 K and an activation energy calculated as 35.09 kJ/mol. Ghodke et al.[16] described the synthesis of nickel nanoparticles as a catalyst for hydrogen production, which in turn showed a 300 K HGR value of 255 mL_{H2} min^{-1} g_{cat}^{-1} and activation energy of 69.76 kJ/mol. The FeCo-B catalyst, B indicates the presence of boron, described by Balbay et al.[17] showed excellent catalytic activity for dehydrogenating $NaBH_4$, 4536 mL H_2 min^{-1} g_{cat}^{-1}.

Studies indicate that many catalysts based on the aforementioned metals are manufactured by pyrolysis or chemical reduction of the adsorbed metal on the surface of different substrates[16,18,19]. These catalysts often show aggregation during the pyrolysis or reduction. To overcome this defect, organic metal structures (MOFs) have often been used as metal precursors for catalytic preparation[20-22]. MOFs are hybrid crystalline materials consisting of ions or metal clusters coordinated with multidentate organic molecules, giving rise to porous, well-defined, and stable structures with large surface areas and flexible adaptability. The metal species in these catalysts are generally well distributed and immobilized against migration, resulting in improved catalyst performance[23,24].

The literature covers numerous MOFs applied in catalysis, particularly for the MIL-100 (Fe), which is widely studied due to its mesoporous cages, large surface area, and many coordinatively unsaturated metal sites[25]. Han et al.[25] synthesized MIL-100(Fe) without solvent and without hydrofluoric acid, which exhibited catalytic performance in the acetalization of benzaldehyde with methanol, producing 93% of dimethyl acetate of benzaldehyde and maintaining its initial activity after five cycles. Wang et al.[26] described the efficiency of MIL-100(Fe) in catalytic removal of ozone. The MOF demonstrated a durable 100% ozone conversion efficiency for over 100 hours under conditions of 45% relative humidity. Nivetha et al.[27] synthesized the MIL-100(Fe) MOF using a modified hydrothermal method, without the use of hydrofluoric acid (HF). The synthesized material was investigated as an electrocatalyst for the hydrogen evolution reaction, demonstrating excellent performance in both acidic and alkaline media. The electrochemical results showed low Tafel slope values (53.59 and 56.65 mV dec^{-1}, high exchange current densities (76.44 and 72.75 mA cm^{-2}), low overpotentials (148.29 and 150.57 mV), and good long-term stability, with the high activity attributed to its large surface area and porous nature.

Amouzesh et al.[28] present a strategy to enhance photocatalytic efficiency for water splitting under ultraviolet light by incorporating ZnO nanoparticles into the MIL-100(Fe) framework through atmospheric pressure atomic layer deposition (ALD). The ZnO/MIL-100(Fe) composite, prepared via a 1-cycle ALD process, exhibited higher hydrogen evolution rates of 8465 $\mu mol\, g^{-1} h^{-1}$ and improved durability.

This article presents the synthesis and characterization of the MOF MIL-100(Fe) using two different solvents: water and DMF. The resulting products were utilized as catalysts for hydrogen production through the hydrolysis of sodium borohydride. We analyzed how the different synthetic approaches affected the catalytic properties of the materials.

2. Experimental Section

2.1. Materials and methods

Reactants and solvents were used as received without further purification. Iron (III) nitrate nonahydrate ($Fe(NO_3)_3.9H_2O$) and benzene-3.5-tricarboxylic acid (H_3BTC) were acquired from Sigma-Aldrich. Sodium hydroxide (NaOH), ethanol (EtOH), and N,N-dimetylformamide (DMF) were acquired from Dynamics. Iron(II) sulfate heptahydrate ($FeSO_4.7H_2O$) was acquired from Vetec.

2.2. Conventional synthesis of MIL-100 (Fe)_S

In a typical solvothermal procedure, 0.0016 mol of Iron (III) nitrate nonahydrate ($Fe(NO_3)_3.9H_2O$) and 0.0013 mol of benzene-1,3,5-tricarboxylic acid (H_3BTC) were dissolved in 30 mL of N, N-dimethylformamide. The mixture was stirred for 20 minutes and then transferred to a Teflon reactor, where it was heated to 150 °C for 24 hours in an autoclave. After washing with DMF and ethanol three times each, the obtained orange powder was dried in a vacuum at 60 °C for 22 hours. This sample has been designated as MIL-100(Fe)_S.

2.3. Green synthesis of MIL-100 (Fe)_G

The green synthetic approach eliminates harmful solvents, including DMF, and high temperatures and pressures. Instead, we utilized distilled water at room temperature. First, sodium trimesate (Na_3BTC) was prepared by mixing 0.0068 mol of H_3BTC and 0.02 mol of sodium hydroxide (NaOH) in 125 mL of distilled water, followed by sonication until complete dissolution. The solution was filtered to remove any unreacted H_3BTC, and 50 mL of ethanol was added to the filtrate to precipitate sodium trimesate (Na_3BTC). The obtained compound was filtered and washed with ethanol to remove unreacted NaOH and then diethyl ether. The soft, light white powder was dried overnight in an oven at 45 °C.

To synthesize MIL-100(Fe), 0.0063 mol of Na_3BTC was added in 125 mL of distilled water. A second solution was prepared by dissolving 0.0081 mol of Iron (II) sulfate heptahydrate ($FeSO_4.7H_2O$) in 125 ml of water. Both solutions were then mixed and allowed to react in the presence of air for 15 hours at room temperature. Finally, the precipitate was separated from the supernatant liquid by centrifugation and washed three times with water and three times with ethanol.

The solid was then dried in a vacuum oven at 70 °C for 12 hours. This sample has been designated as MIL-100(Fe)_G.

2.4. Characterization

Powder X-ray Diffraction (PXRD) analyses were performed using a Rigaku SmartLab diffractometer equipped with a D/Tex Ultra 250 detector. The radiation employed was Cu Kα (λ = 1.5406 Å), filtered through a nickel filter, with a current setting of 30 mA and a voltage of 40 kV. The diffractograms were recorded in increments of 0.01° from 5° to 60° (2θ). The crystallite sizes were estimated using the Scherrer equation[29]. The simulated diffractograms were calculated using the corresponding crystallographic data and the Mercury software version 3.8. Attenuated Total Reflectance Fourier Transform Infrared (ATR-FTIR) spectroscopy was performed using a Bruker Vertex 70/v spectrometer. The samples were analyzed over the range of 500-4000 cm^{-1}. The TGA/DTA curves were measured from 25 to 800 °C at a heating rate of 10 °C/min using a Shimadzu TGA 50 thermal balance (DTG-60H), under synthetic air with a flow rate of 50 mL/min. Scanning Electron Microscopy (SEM) images were taken using a high-resolution MIRA 3 TESCAN apparatus operating at an acceleration voltage of 15 kV. The surface area of the catalysts was determined from nitrogen adsorption-desorption curves obtained at 77.3 K using Quantachrome Autosorb-iQ instruments and the BET method. Before the measurements, the samples were degassed at 80 °C for 24 hours in a vacuum oven.

2.5. Hydrogen generation experiments

The experiments for H_2 production were conducted in triplicate at temperatures of 300.15, 320.15, and 340.15 K, using the water displacement method[30]. In a typical procedure, 40 mg of catalyst was added to a two-neck flask. Next, a solution of $NaBH_4$ (40 mg dissolved in 10 mL of water) was introduced into the flask using a syringe, while keeping the mixture under magnetic stirring for 40 minutes. During this time, the volume of hydrogen gas (H_2) produced was quantified by measuring the corresponding water displacement in the system.

The hydrogen evolution was monitored by measuring the time required to reach specific, predetermined volumes of H_2 gas during each experiment. Rather than recording the cumulative volume of hydrogen at regular time intervals, the methodology was designed to determine how long it took for the reaction to generate fixed amounts of hydrogen. As a result, the time variable was treated as the independent variable in the data plots. Accordingly, error bars were assigned to the time axis, reflecting the variation observed across experimental replicates in the duration required to produce each target volume.

To determine the stability of the catalyst, the catalytic reactions were repeated by performing cycles. For each cycle, another equivalent amount of $NaBH_4$ (40 mg) was added to the mixture after the previous cycle with no catalyst regeneration. The volume of hydrogen produced was measured during the following 40 minutes. For the most promising material, the effects of varying the catalyst amount (30, 40, and 50 mg) and $NaBH_4$ (30, 40, 50, and 60 mg) were evaluated at a temperature of 300.15 K. The Hydrogen Generation Rate (HGR) was calculated using Equation 2, taking into account the volume of H_2 produced from the linear portion of the graph, divided by time, and the mass of the catalyst.

$$HGR = \frac{V_{H_2}}{t \times m_{cat}} \tag{2}$$

where: V_{H_2} is the volume of hydrogen generated during $NaBH_4$ hydrolysis (mL), t is the time (min), and m_{cat} is a catalyst mass (g).

Using the Arrhenius equation (Equation 3), the activation energy for the hydrolysis reaction catalysed by MIL-100(Fe)_S and MIL-100(Fe)_G is determined:

$$\mathrm{Ln}(k) = -\frac{E_a}{R}\frac{1}{T} + Ln\ A \tag{3}$$

In this equation, k stands for the rate constant (s^{-1}), A is the pre-exponential factor, Ea is the activation energy (J mol^{-1}), R is the universal gas constant (8.314 J mol^{-1} K^{-1}), and T is the absolute temperature (K).

Hydrogen generation rates were measured at various temperatures while maintaining all other experimental conditions constant. The rate constant (k) was obtained from the slope of the hydrogen volume versus time curve, focusing on the initial stage of the reaction, where the rate is maximal and exhibits linear behavior. The natural logarithm of k (ln k) was then plotted as a function of the inverse absolute temperature (1/T), yielding a linear trend with a slope corresponding to $-E_a/R$. From this slope, the activation energy (E_a) was calculated for each catalyst[31].

3. Results and Discussion

3.1. ATR-FTIR

Figure 1 presents the ATR-FTIR spectra of the MIL-100(Fe)_S and MIL-100(Fe)_G samples, along with

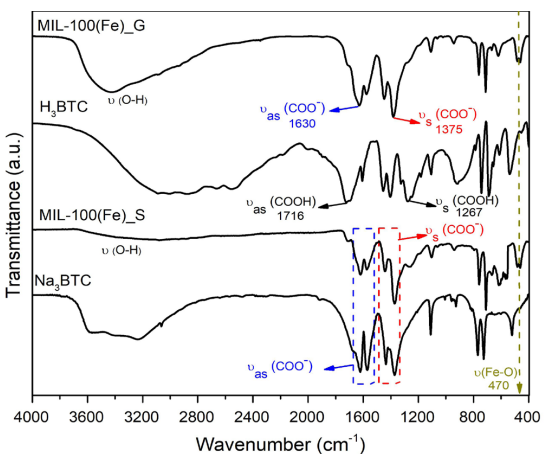

Figure 1. ATR-FTIR spectra of the MIL-100(Fe)_S and MIL-100(Fe)_G samples, along with the ligand precursors H_3BTC and Na_3BTC.

the ligand precursors H_3BTC and Na_3BTC. The spectra of MIL-100(Fe)_S and MIL-100(Fe)_G exhibit a broadband between 3100 and 3500 cm^{-1}, associated with the stretching vibrations ν(O−H), which originate from water molecules coordinated to the open metal sites in the MIL-100(Fe) framework[32].

The FTIR spectrum of H_3BTC (benzene-1,3,5-tricarboxylic acid) displays characteristic bands at 1716 cm^{-1} and 1267 cm^{-1}, corresponding to the stretching vibrations of the protonated carboxyl group (-COOH). Specifically, the band at 1716 cm^{-1} is attributed to the C=O stretching (ν(C=O)), while the band at 1267 cm^{-1} arises from C-O stretching (ν(C-O))[32].

In the FTIR spectrum of MIL-100(Fe)_G and MIL-100(Fe)_S, the C=O and C-O bands are absent, as the carboxyl groups of the ligand have been completely deprotonated and coordinated to the iron centers. Consequently, the bands observed at 1630 cm^{-1} and 1375 cm^{-1} in MIL-100(Fe)_G and 1620 cm^{-1} and 1371 cm^{-1} in MIL-100(Fe)_S are assigned to the asymmetric $\nu_{as}(COO^-)$ and symmetric $\nu_s(COO^-)$ stretching vibrations of the carboxylate anion (COO^-), respectively, confirming its coordination with the iron ions and the formation of the MOF structure. The difference between the symmetric and asymmetric vibrations, with values greater than 200 cm^{-1} ($\Delta\nu$ = 255 and 249 cm^{-1}), suggests that the carboxylates adopt a monodentate coordination mode[33].

The FTIR spectra of Na_3BTC, MIL-100_S, and MIL-100_G exhibit strong similarities, particularly in the regions associated with carboxylate vibrations. This close resemblance between the spectrum of Na_3BTC (the fully deprotonated form of H_3BTC) and the spectra of both MIL-100(Fe) samples confirms the deprotonation of the H_3BTC ligand and indicates its coordination with the iron ions. The coordination involving carboxylate groups aligns with the anticipated structure of MIL-100(Fe), as described in the introduction, where organic ligand acts as a bridge between the iron octahedral trimers[32,34]. Additionally, the vibration observed around 470 cm^{-1} for both structures can be attributed to the Fe-O stretch, which occurs as the oxygen atom coordinates with the iron ions[31,35,36].

3.2. PXRD

The experimental diffraction patterns of samples MIL-100(Fe)_S and MIL-100(Fe)_G, along with the simulated diffraction pattern of MIL-100(Fe), are shown in Figure 2. The simulated pattern, calculated from the crystallographic data obtained in the CCDC file #640536, matches well with the experimental patterns[31,37,38]. The crystalline structure of MIL-100(Fe), as described in the literature, consists of iron octahedral trimers that share a common vertex, μ3-O. These trimers are interconnected by benzene-1,3,5-tricarboxylate, or H_3BTC, forming super-tetrahedrons that cluster into a Mobil Thirty-Nine zeolite architecture[35,37].

It is worth noting that the diffraction peaks in the MIL-100(Fe)_S pattern are broader than those observed in the MIL-100(Fe)_G pattern. The width of the band, known as Full-Width at Half Maximum (FWHM), was used to calculate the crystallite size using the Scherrer equation. The average crystallite size calculated for the samples MIL-100(Fe)_S and MIL-100(Fe)_G were 6.1 and 25 nm, respectively.

3.3. Thermal analysis

TG-DTA curves of synthesized powders are shown in Figure 3. The TG curve of the MIL-100(Fe)_S sample shows three mass loss events in the temperature range of 25-800 °C. The first mass loss of 7.56%, an endothermic event, occurred between 42.4-104.83 °C and was related to the evaporation of water and ethanol, both on the surface and within the material's porosity. The second mass loss (33.91%) from 315.10 to 504.81 °C corresponds to the decomposition of coordinated organic ligands due to structural breakdown, an exothermic event. The final mass loss (9.36%), an endothermic event, refers to the collapse of the MIL-100(Fe) structure due to the complete removal of organic linkers[35,39,40].

Two stages of thermal decomposition were observed for MIL-100(Fe)_G, as shown in Figure 3. The first stage, with a 32.02% mass loss, is due to the removal of physisorbed water, an endothermic event. In the

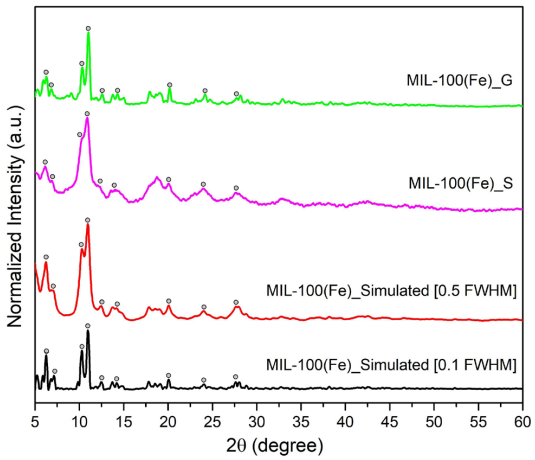

Figure 2. PXRD patterns of synthesized MIL-100(Fe)_S and MIL-100(Fe)_G samples compared to simulated PXRD patterns of MIL-100(Fe) calculated using FWHM values of 0.1 and 0.5.

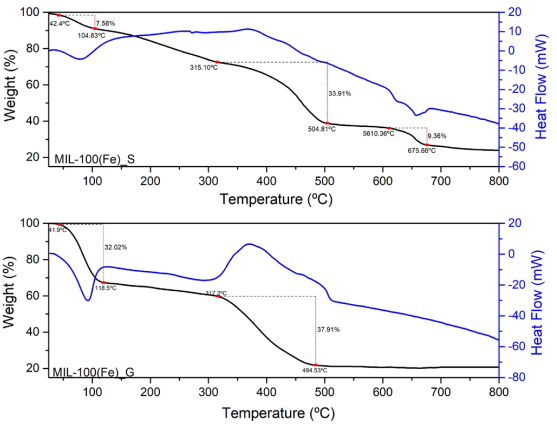

Figure 3. TG-DTA profiles of (a) MIL-100(Fe)_S and (b) MIL-100(Fe)_G samples.

temperature range of approximately 100 to 300 °C, the TG curve was slightly inclined downward, indicating that the MOF was relatively stable. The second stage, which involves a mass loss of 37.91%, is an exothermic event associated with the organic ligand's combustion and the MOF structure's collapse[26,34].

3.4. Scanning Electron Microscopy (SEM)

Scanning electron microscopy was used to characterize the morphology of the MIL-100 samples prepared through various synthetic approaches, with the corresponding images displayed in Figure 4.

The MIL-100_S material, synthesized via a conventional solvothermal route, exhibits well-defined microcrystals with smooth surfaces that aggregate into uneven clusters with an average size of 97 µm. In contrast, the MIL-100_G sample, obtained via a green synthetic method, displays particles with a predominantly octahedral morphology, although some smaller, irregularly shaped particles are also observed. The average particle size for the MIL-100_G material is significantly smaller, measuring approximately 0.183 µm. This difference in morphology and particle size between the two samples highlights the influence of the synthesis method on the final product[33,36].

3.5. BET

The textural properties of the MIL-100(Fe) samples, as determined by BET analysis, are presented in Table 1. The MIL-100(Fe)_G sample, synthesized via a green method and at room temperature, exhibits a significantly higher surface area and total pore volume than the solvothermally synthesized MIL-100(Fe)_S material. This substantial difference is attributed to the distinct synthesis conditions

Table 1. Textural properties of pristine MIL-100(Fe)_S and MIL-100(Fe)_G.

Sample	Surface area (BET) (m^2g^{-1})	Total pore volume (cc g^{-1})
MIL-100(Fe)_S	71.820	0.4860
MIL-100(Fe)_G	1224.337	0.7168

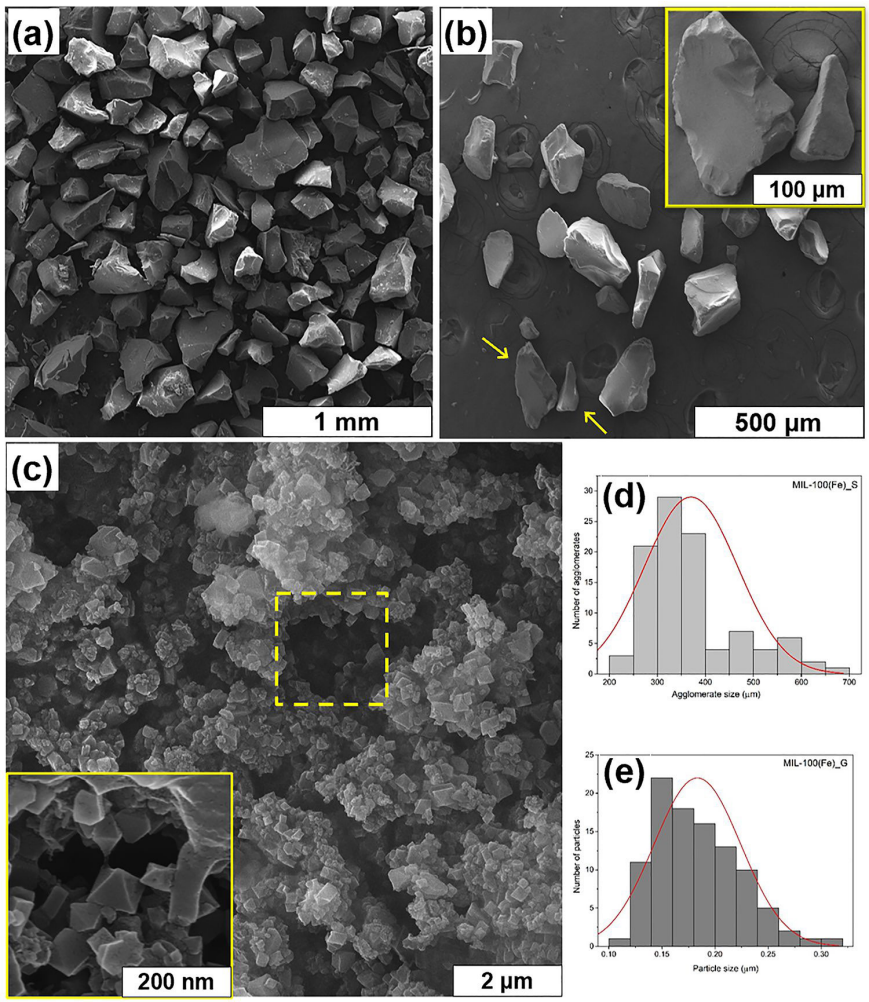

Figure 4. SEM micrographs of (a)-(b) MIL-100(Fe)_S, (c)-(d) MIL-100(Fe)_G, and the particle size distribution of (d) MIL-100(Fe)_S and (e) MIL-100(Fe)_G.

employed. The green synthesis approach likely favors more extensive crystallization and the development of a more porous framework, resulting in a larger surface area and pore volume. Furthermore, as with any other type of material, the MOF particle size is inversely related to the surface area-to-volume ratio[41]; that is, decreasing particle size results in a greater surface area. This enhanced porosity in MIL-100(Fe)_G suggests a greater potential for applications in catalysis and adsorption processes, where a high surface area and accessible pore volume are crucial for efficient performance.

3.6. Catalytic activity in the hydrolysis of sodium borohydride

To investigate the catalytic activity of MIL-100(Fe) in the hydrolysis of sodium borohydride ($NaBH_4$), hydrogen production experiments were conducted at various temperatures (300.15 K, 320.15 K, and 340.15 K) for 40 minutes, using 40 mg of catalyst. Control experiments, performed in the absence of a catalyst, yielded low hydrogen production volumes: 7 mL, 10 mL, and 16 mL at 300.15 K, 320.15 K, and 340.15 K, respectively. These low yields underscore the importance of a catalyst for efficient hydrogen generation. Introducing MIL-100(Fe) significantly enhanced hydrogen production (see Figure 5).

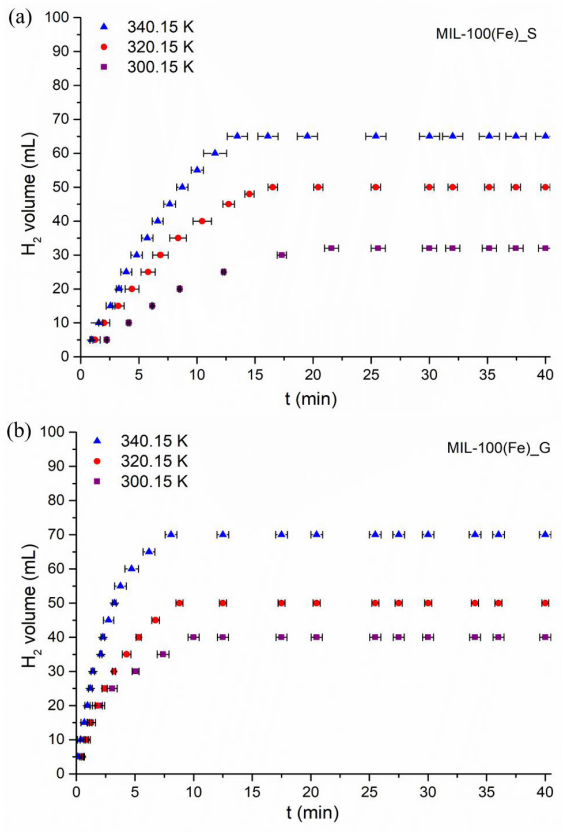

Figure 5. Hydrogen generation from the hydrolysis of $NaBH_4$ catalyzed by (a) MIL-100(Fe)_S and (b) MIL-100(Fe)_G at different temperatures (catalyst mass: 40 mg).

The MIL-100_G catalyst, synthesized via a green method, exhibited superior performance at all investigated temperatures. At 300.15 K (near room temperature), MIL-100_G generated 40 mL of H_2 within 10 minutes, corresponding to a reaction efficiency of 38.46%. Under the same conditions, the solvothermally synthesized MIL-100_S catalyst produced 32 mL of H_2 in 21.58 minutes, achieving a reaction efficiency of 30.77%.

As expected, the hydrogen generation rate (HGR) increases with increasing reaction temperature due to the enhanced kinetics of $NaBH_4$ hydrolysis. Elevated temperatures increase the kinetic energy of the reactants, leading to more frequent and energetic collisions between $NaBH_4$ and the active sites of the catalyst. This, in turn, accelerates the hydrolysis reaction, resulting in higher hydrogen generation rates. The analysis of the hydrogen evolution profiles indicates that the hydrolysis of $NaBH_4$ catalyzed by MIL-100(Fe)_S follows pseudo-first-order kinetics, whereas the reaction catalyzed by MIL-100(Fe)_G exhibits zero-order kinetics. Table 2 presents the rate constants (k) obtained from the fitting of pseudo-first-order and zero-order kinetic models to the experimental data collected at 300.15 K.

The Arrhenius equation (Equation 3) was used to determine the activation energy (Ea) for the hydrolysis reaction of $NaBH_4$ using MIL-100(Fe)_S and MIL-100(Fe)_G. The MIL-100(Fe)_S catalyst has an activation energy of 19.0 kJ mol^{-1}, while the MIL-100(Fe)_G has an activation energy of 16.2 kJ mol^{-1}. Figure 6 shows the Arrhenius plot for both catalysts.

The Ea values provide important information about the energy barrier associated with the reaction. The lower the value, the more easily the reaction can occur at lower temperatures. Table 3 summarizes all the data related to

Table 2. Parameters obtained from the pseudo-first-order and zero-order kinetic models fitted to the experimental data at 300.15 K.

Sample	Kinetic Model	k (mL min^{-1})	R^2
MIL-100(Fe)_S	Zero-order	0.10	0.981
MIL-100(Fe)_S	Pseudo-first-order	0.26	0.993
MIL-100(Fe)_G	Zero-order	0.33	0.993
MIL-100(Fe)_G	Pseudo-first-order	1.26	0.904

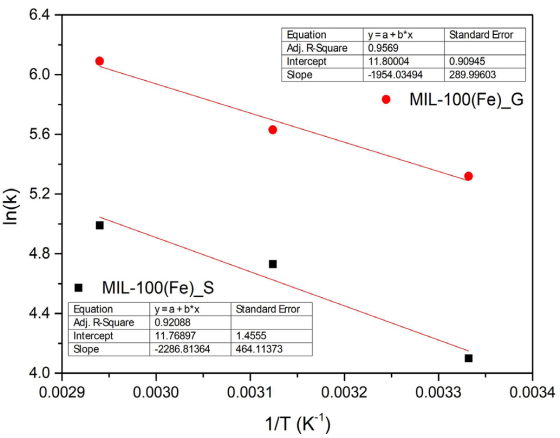

Figure 6. Arrhenius plot for MIL-100(Fe)_S and MIL-100(Fe)_G.

Table 3. Catalytic performance of MIL-100(Fe)_S and MIL-100(Fe)_G in the hydrolysis of $NaBH_4$.

Catalyst	T (K)	HGR	Efficiency	Ea
		(mL min^{-1} g_{cat}^{-1})	(%)	(kJ mol^{-1})
MIL-100(Fe)_S	300.15	60.39	30.77	19.0
	320.15	113.38	48.08	
	340.15	146.96	62.50	
MIL-100(Fe)_G	300.15	204.25	38.46	16.2
	320.15	278.55	48.08	
	340.15	443.46	67.31	

hydrogen production using the two catalytic systems, MIL-100(Fe)_S and MIL-100(Fe)_G.

The superior performance of the MIL-100(Fe)_G catalyst can be attributed to differences in their structural and surface properties arising from the distinct synthesis conditions.

The elevated temperatures employed in the solvothermal method promote rapid crystal nucleation and growth, resulting in larger, well-defined crystals with a more homogeneous particle size distribution, as confirmed by SEM analysis. However, this accelerated growth can limit the development of porosity by leading to pore collapse or partial blockage due to densification of the framework, resulting in a low specific surface area of 72 m^2/g. In contrast, the green approach synthesis performed at room temperature results in a slower nucleation rate and smaller crystals, creating a more porous and irregular microstructure, which leads to a higher surface area of 1224 m^2/g. This structure features an open-pore network that enhances the diffusion of sodium borohydride and water, improving reaction efficiency. Smaller crystals also increase the number of structural defects, providing additional active sites for the hydrolysis reaction. Consequently, the high specific surface area of the catalyst significantly boosts its catalytic activity, contributing to its superior performance.

Additional experiments were conducted to evaluate the recyclability of the catalysts. It is worth noting that the catalysts were not regenerated between cycles, and all analyses were carried out at 300.15 K. The results indicate that the MOF MIL-100(Fe)_S sustained catalytic hydrogen generation over four cycles, though with a gradual decline in performance. Conversely, the MOF MIL-100(Fe)_G demonstrated greater stability, maintaining hydrogen production across five consecutive cycles, as illustrated in Figure 7.

This decline indicates the structural degradation of the MOF during the reaction, as well as the formation of by-products such as the magnetite (Fe_3O_4) and the tincalconite ($Na_2[B4O_5(OH)_4]\cdot 3H_2O$), along with morphological changes including loss of crystallinity and a reduction in particle size. In contrast, MIL-100(Fe)_G demonstrated greater structural stability and maintained catalytic activity over five cycles, likely due to differences in microstructure and crystallinity that delay degradation.

Given the promising results obtained with the MIL-100(Fe)_G catalyst, this material was chosen to investigate the effects of varying the mass of $NaBH_4$ and the catalyst on the catalytic hydrolysis of sodium borohydride at 300.15 K. The results are shown in Figure 8.

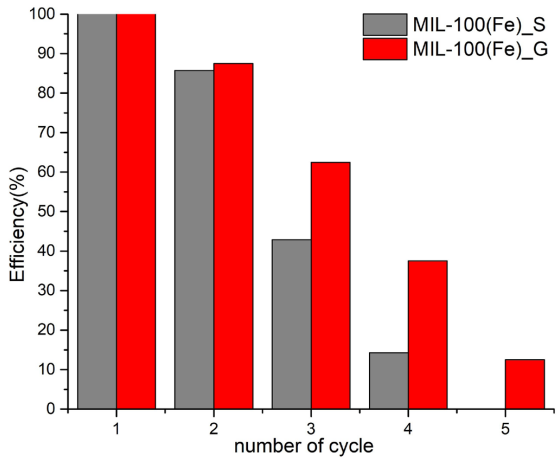

Figure 7. Recyclability of the samples MIL-100(Fe)_S and MIL-100(Fe)_G. Percentage values associated with the maximum efficiency achieved in the first cycle.

Figure 8a shows how the concentration of $NaBH_4$ affects the rate of hydrogen generation. Data analysis indicates that hydrogen production increases as the amount of $NaBH_4$ rises, aligning with the theoretical expectation that higher $NaBH_4$ availability leads to increased H_2 production. Moreover, Figure 8b demonstrates a clear enhancement in the Hydrogen Generation Rate (HGR) with increasing $NaBH_4$ concentrations. The HGR values of 179.08, 204.25, 284.09, and 314.46 L min^{-1} g_{cat}^{-1} were obtained for 30, 40, 50, and 60 mg of $NaBH_4$, respectively.

This progressive increase suggests that within the tested range, the catalytic system operates efficiently without significant mass transfer limitations or saturation effects. The increased availability of $NaBH_4$ molecules likely increases the frequency of collisions and the local concentration near the catalyst surface, facilitating faster hydrogen evolution[42].

Figure 9a shows the results of the analysis of the impact of catalyst mass on hydrogen production using 30, 40, and 50 mg of MIL-100(Fe)_G. Increasing the amount of catalyst positively affected the Hydrogen Generation Rate (HGR) values, as shown in Figure 9b. However, the reaction yield remained constant at 38.46%, except for the 30 mg sample, which yielded 24.04%.

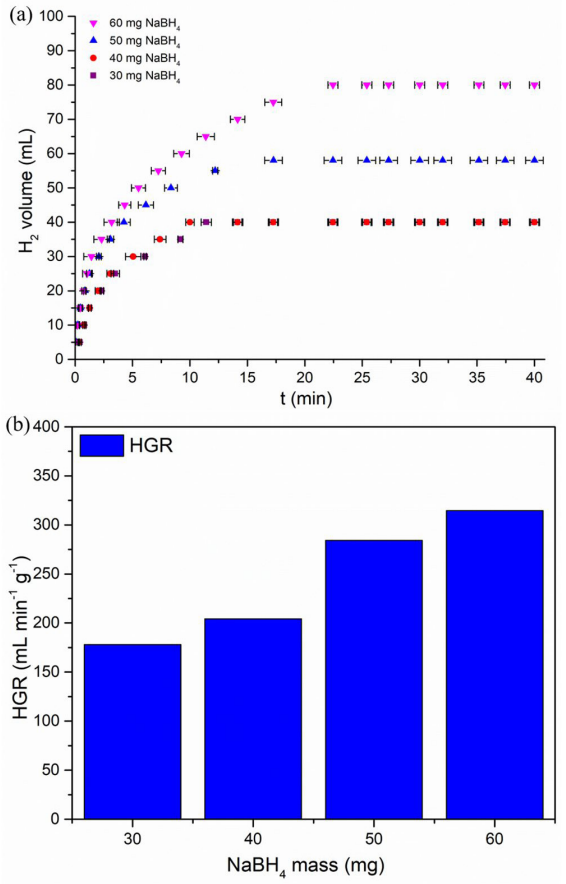

Figure 8. NBH_4 hydrolysis in the presence of MIL-100(Fe)_G catalyst: (a) Hydrogen generation with varying amounts of $NaBH_4$ at 300.15 K; and (b) The effect of $NaBH_4$ quantity on the hydrogen generation rate (300.15 K, catalyst mass: 40 mg).

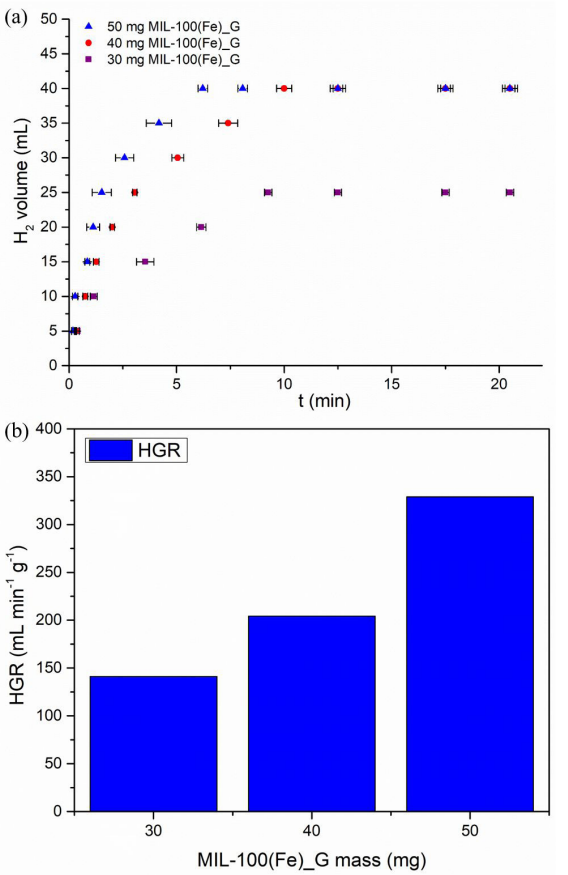

Figure 9. (a) Hydrogen generation by varying the mass of MIL-100(Fe)_G. (b) The influence of MIL-100(Fe)_G mass on the hydrogen generation rate (300.15 K, $NaBH_4$ mass: 40 mg).

The lower yield observed with 30 mg of catalyst and an HGR of 141.24 mL min^{-1} g_{cat}^{-1} indicates that this amount cannot catalyze the reaction efficiently. In contrast, 50 mg of catalyst resulted in the highest HGR, 328.95 mL min^{-1} g_{cat}^{-1}, due to the shorter time required for H_2 production. However, no significant improvement in efficiency was observed compared to 40 mg of MIL-100(Fe)_G. Thus, using 50 mg of catalyst may lead to unnecessary waste of catalytic material, as the H_2 production did not exceed 40 mL, indicating that the amount of $NaBH_4$ limits the reaction.

3.6.1. Characterization of the spent catalysts

Figure 10 presents the PXRD patterns of the spent catalyst alongside the calculated tincalconite ($Na_2[B_4O_5(OH)_4]\cdot 3H_2O$) diffractogram.

The experimental patterns exhibit intense and well-defined diffraction peaks of tincalconite (COD file #2000170), a byproduct resulting from the hydrolysis of sodium borohydride ($NaBH_4$). The absence of MIL-100 diffraction peaks in the spent catalyst diffractograms indicates complete conversion of the MOF structure into magnetite (Fe_3O_4). The diffraction peaks marked with a small circle align well with the main peaks of magnetite (JCPDS file #19-629).

The spent catalysts were also characterized using SEM. The micrographs of sample MIL-100(Fe)_S are shown in

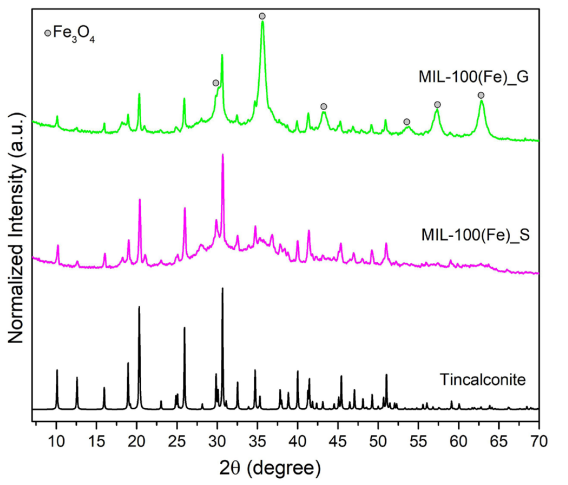

Figure 10. PXRD patterns of the spent catalysts MIL-100(Fe)_S and MIL-100(Fe)_G, along with the calculated diffractogram of tincalconite.

Figures 11a and 11b, indicating that, compared to the pristine sample, there was a significant decrease in agglomerate size, dropping from values above 100 µm to below 5 µm. A closer examination of these agglomerates reveals a rougher, more irregular surface with

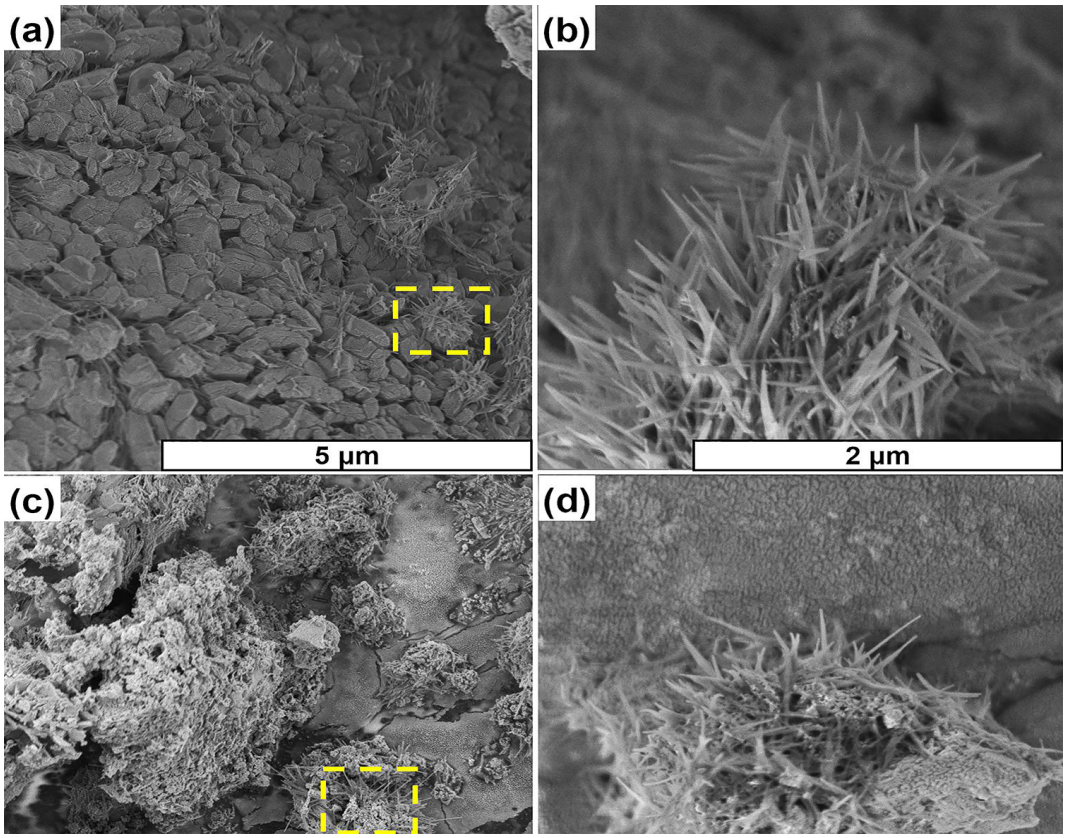

Figure 11. SEM micrographs of the spent catalysts (a)-(b) MIL-100(Fe)_S and (c)-(d) MIL-100(Fe)_G.

Table 4. Comparison of activation energy (Ea) values for various catalysts in the hydrolysis reaction of sodium borohydride ($NaBH_4$).

Catalysts	$NaBH_4$ (wt%)	NaOH (wt%)	Reaction temperature (°C)	Ea, kJ mol^{-1}	HGR mL min^{-1} g^{-1}	References
Fe/SiO_2	5	10	RT	59	130	[44]
Fe_2O_3@OMWCNTs	1	-	RT	15.96	1368	[45]
Co-Fe-B	5	0.1	RT	55.6	1069.3	[46]
Ni-Fe-B	15	5	RT	27	221	[47]
FeB-Ni_3B	0.75	8	RT	69.6	90.90	[48]
Fe–Fe_2B	1.0	0.1	RT	38	140	[49]
MIL-100(Fe)_S	0.4	-	RT	19	60.39	This work
MIL-100(Fe)_G	0.4	-	RT	16.2	204.25	This work

RT: Room Temperature

visible fissures. Additionally, a second microstructure is observed, characterized by rod-like crystals.

The micrograph of the spent sample MIL-100(Fe)_G displays two distinct microstructures: the first is characterized by porous agglomerates with irregular surfaces, while the second comprises rod-like crystals, likely associated with the crystalline phases identified by PXRD, tincalconite, and magnetite[43].

Table 4 summarizes the hydrogen production rates and activation energies (Ea) reported in the literature for $NaBH_4$ hydrolysis catalyzed by various Fe-based materials. While Fe-based catalysts have generally demonstrated promising activity, the use of MIL-100(Fe) for this application has not been previously reported. As a result, the findings presented here make a unique contribution to the field, expanding the scope of Fe-based catalysts for hydrogen production from the hydrolysis of $NaBH_4$. Notably, MIL-100(Fe)_G exhibited an outstanding balance between catalytic activity and a low energy barrier, even under mild reaction conditions and without the use of alkaline additives. Compared to other Fe-based catalysts operating under harsher conditions, MIL-100(Fe) materials display competitive or superior

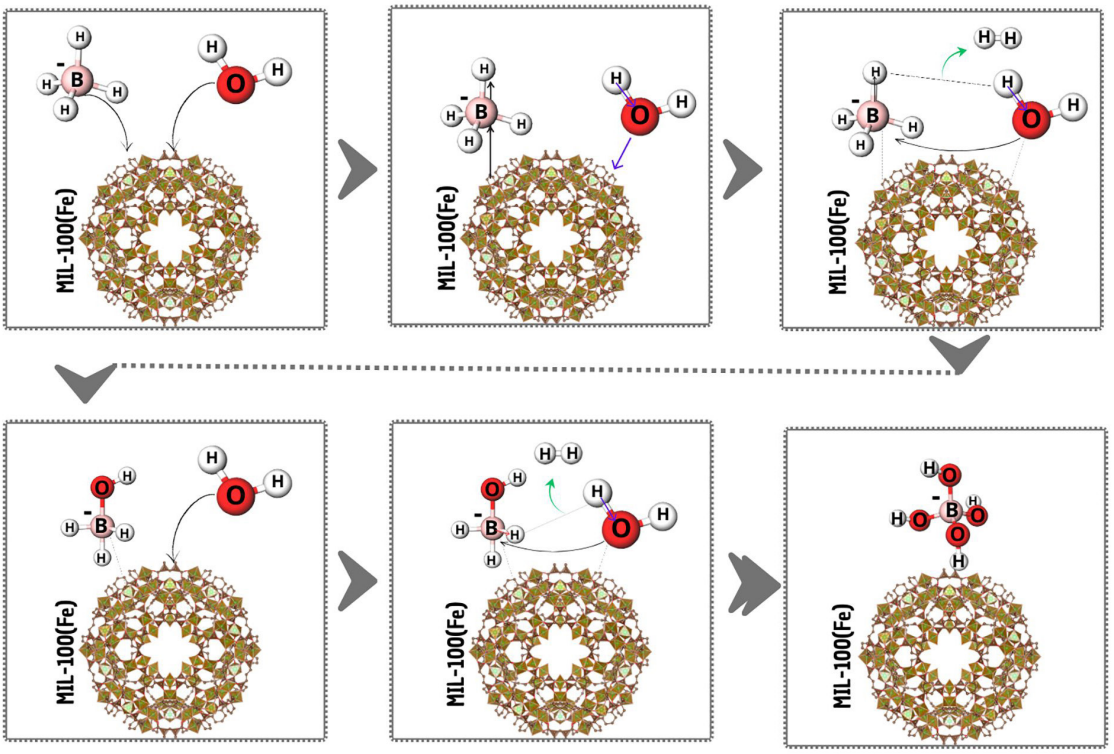

Figure 12. Proposed mechanism for hydrolysis of NaBH4 on the surface of the MOF MIL-100(Fe).

performance, reinforcing their potential as efficient and sustainable alternatives for hydrogen generation.

3.6.2. Mechanism of the dehydrogenation of $NaBH_4$

The hypothetical mechanism is based on the studies of Demirci and Miele[50] and Ekinci[51]. The first step consists of the adsorption of $NaBH_4$ on the catalyst's surface. Adsorption can occur directly with Fe^{3+} ions, which can coordinate with $NaBH_4$ molecules, activating the B-H (borohydride) bond and/or through functional groups such as -OH. In this way, the proposed mechanism explains how the adsorption of the reagents occurs involving the OH groups linked to the metal ion.

The dissociation of sodium borohydride produces BH_4^- and Na^+ ions. The hydrogens from the hydroxyl groups on the surface are evidently protic, so it is believed that BH_4^- adsorbs on the surface layer through interactions between the B of the reagent and the oxygen of the O-H group.

The second stage is the hydrolysis of the three-remaining adsorbed BH_3 hydrides, (OH)-BH_3. Is there a possibility that the adsorbed water could promote the hydrolysis of the adsorbed BH_3. In this case, the reaction mechanism is consistent with the Langmuir-Hinshelwood model. Due to its partially positive charge, Fe^{3+} ions attract polar molecules, such as water (H_2O), which has an asymmetric charge distribution. This polarity allows the oxygen in water to be attracted to the electron-deficient Fe^{3+} ions on the surface of MIL-100(Fe). The interaction between H_2O and Fe^{3+} stabilizes the adsorption of water on the surface of the MOF. This stabilization is crucial to ensure that water molecules remain adsorbed and available for subsequent reactions. The proposed mechanism is depicted in Figure 12.

The gaseous hydrogen formed can reduce the Fe^{3+} ions present in MIL-100(Fe) to Fe^{2+}. After the reduction, the Fe^{2+} and Fe^{3+} ions can combine with the available oxygen to form magnetite Fe_3O_4. Therefore, the conversion of MIL-100(Fe) into Fe_3O_4, indicated by the analysis of the post-catalysis catalysts, may alter the catalytic properties of the materials.

4. Conclusions

This study examined the effectiveness of MIL-100(Fe) produced through conventional solvothermal (MIL-100(Fe)_S) and green synthesis (MIL-100(Fe)_G) methods for catalyzing the hydrolysis of $NaBH_4$ to generate hydrogen. Characterizations using PXRD and SEM confirmed the successful synthesis of MIL-100(Fe). The MIL-100(Fe)_G sample exhibited a higher average crystallite size and smaller particle size than the MIL-100(Fe)_S sample. MIL-100(Fe) materials demonstrated catalytic activity for hydrogen production from $NaBH_4$ hydrolysis at 300.15 K. The MIL-100(Fe)_G catalyst exhibited significantly higher catalytic activity, achieving a hydrogen generation rate of 443.46 $mL \cdot min^{-1} \cdot gcat^{-1}$ with 67.31% yield at 340.15 K and an activation energy of 16.2 $kJ \cdot mol^{-1}$. This superior performance is attributed to its smaller particle size and considerably higher surface area (1224.337 $m^2 \cdot g^{-1}$) compared to the MIL-100(Fe)_S (71.820 $m^2 \cdot g^{-1}$). While the MIL-100(Fe)_G catalyst demonstrated reusability for at least five cycles at 300.15 K without regeneration, a gradual

decrease in catalytic activity was observed. Post-reaction analyses revealed the formation of tincalconite (a hydrated sodium borate) on the catalyst surface, likely blocking active sites and contributing to the activity decline. Although the literature on iron-based catalysts for hydrogen production is limited, this study highlights their potential. It emphasizes that the synthetic method has a significant influence on catalytic performance and impacts the material's microstructural properties, thereby affecting its catalytic activity.

5. Acknowledgments

The authors thank the National Council for Scientific and Technological Development (CNPq, Brazil, process no. 314590/2021-8) and the Coordination for the Improvement of Higher Education Personnel (CAPES) for the financial support.

6. References

1. Uddin K. Nuclear energy, environment and public safety: north-south politics. Strateg Plann Energy Environ. 2019;38(4):31-41. http://doi.org/10.1080/10485236.2019.12054410.
2. Megía PJ, Vizcaino AJ, Calles JA, Carrero A. Hydrogen production technologies: from fossil fuels toward renewable sources. a mini review. Energy Fuels. 2021;35(20):16403-15. http://doi.org/10.1021/acs.energyfuels.1c02501.
3. Ma Y, Wang XR, Li T, Zhang J, Gao J, Sun ZY. Hydrogen and ethanol: production, storage, and transportation. Int J Hydrogen Energy. 2021;46(54):27330-48. http://doi.org/10.1016/j.ijhydene.2021.06.027.
4. Rao PC, Yoon M. Potential liquid-organic hydrogen carrier (LOHC) systems: a review on recent progress. Energies. 2020;13(22):6040. http://doi.org/10.3390/en13226040.
5. Souza ES, Oliveira MA, Santana JJ, Łukasik N, Costa OMMM, Almeida LC, et al. Fabrication of gold and silver nanoparticles supported on zinc imidazolate metal-organic frameworks as active catalysts for hydrogen release from ammonia borane. ACS Omega. 2024;9(39):41084-96. http://doi.org/10.1021/acsomega.4c07068.
6. Winter CJ. Into the hydrogen energy economy: milestones. Int J Hydrogen Energy. 2005;30(7):681-5. http://doi.org/10.1016/j.ijhydene.2004.12.011.
7. Abdin Z, Zafaranloo A, Rafiee A, Mérida W, Lipiński W, Khalilpour KR. Hydrogen as an energy vector. Renew Sustain Energy Rev. 2020;120:109620. http://doi.org/10.1016/j.rser.2019.109620.
8. Umegaki T, Yan JM, Zhang XB, Shioyama H, Kuriyama N, Xu Q. Boron- and nitrogen-based chemical hydrogen storage materials. Int J Hydrogen Energy. 2009;34(5):2303-11. http://doi.org/10.1016/j.ijhydene.2009.01.002.
9. Zhong H, Ouyang LZ, Ye JS, Liu JW, Wang H, Yao XD, et al. An one-step approach towards hydrogen production and storage through regeneration of $NaBH_4$. Energy Storage Mater. 2017;7:222-8. http://doi.org/10.1016/j.ensm.2017.03.001.
10. Jia X, Sang Z, Sun L, Xu F, Pan H, Zhang C, et al. Graphene-modified Co-B-P catalysts for hydrogen generation from sodium borohydride hydrolysis. Nanomaterials. 2022;12(16):2732. http://doi.org/10.3390/nano12162732.
11. Guella G, Zanchetta C, Patton B, Miotello A. New insights on the mechanism of palladium-catalyzed hydrolysis of sodium borohydride from $_{11}$B NMR measurements. J Phys Chem B. 2006;110(34):17024-33. http://doi.org/10.1021/jp063362n.
12. Genç AE, Akc A, Kutlu B. The catalytic effect of the Au (111) and Pt (111) surfaces to the sodium borohydride hydrolysis reaction mechanism: a DFT study. Int J Hydrogen Energy. 2018;43(31):14347-59. http://doi.org/10.1016/j.ijhydene.2018.06.026.
13. Semiz L, Abdullayeva N, Sankir M. Nanoporous Pt and Ru catalysts by chemical dealloying of Pt-Al and Ru-Al alloys for ultrafast hydrogen generation. J Alloys Compd. 2018;744:110-5. http://doi.org/10.1016/j.jallcom.2018.02.082.
14. Oliveira MA, Souza ES, Santana JJ, Łukasik N, Silva BSL, Barros BS, et al. M-BDC (M = Co and/ or Fe) MOFs as effective catalysts for hydrogen generation via hydrolysis of sodium borohydride. Appl Surf Sci. 2023;628:157361. http://doi.org/10.1016/j.apsusc.2023.157361.
15. Lin F, Zhang A, Zhang J, Yang L, Zhang F, Li R, et al. Hydrogen generation from sodium borohydride hydrolysis promoted by MOF-derived carbon supported cobalt catalysts. Colloids Surf A Physicochem Eng Asp. 2021;626:127033. http://doi.org/10.1016/j.colsurfa.2021.127033.
16. Ghodke NP, Rayaprol S, Bhoraskar SV, Mathe VL. Catalytic hydrolysis of sodium borohydride solution for hydrogen production using thermal plasma synthesized nickel nanoparticles. Int J Hydrogen Energy. 2020;45(33):16591-605. http://doi.org/10.1016/j.ijhydene.2020.04.143.
17. Balbay A, Selvitepe N, Saka C. Fe doped-CoB catalysts with phosphoric acid-activated montmorillonite as support for efficient hydrogen production via $NaBH_4$ hydrolysis. Int J Hydrogen Energy. 2021;46(1):425-38. http://doi.org/10.1016/j.ijhydene.2020.09.181.
18. Lee MH, Deka JR, Cheng CJ, Lu NF, Saikia D, Yang YC, et al. Synthesis of highly dispersed ultra-small cobalt nanoparticles within the cage-type mesopores of 3D cubic mesoporous silica via double agent reduction method for catalytic hydrogen generation. Appl Surf Sci. 2019;470(1):764-72. http://doi.org/10.1016/j.apsusc.2018.11.171.
19. Guo Y, Zhang R, Hao W, Zhang J, Yang Y. Multifunctional Co–B–O@CoxB catalysts for efficient hydrogen generation. Int J Hydrogen Energy. 2020;45(1):380-90. http://doi.org/10.1016/j.ijhydene.2019.09.008.
20. Du L, Xing L, Zhang G, Sun S. Metal-organic framework derived carbon materials for electrocatalytic oxygen reactions: recent progress and future perspectives. Carbon. 2020;156:77-92. http://doi.org/10.1016/j.carbon.2019.09.029.
21. Jiao L, Jiang HL. Metal-organic-framework-based single-atom catalysts for energy applications. Chem. 2019;5(4):786-804. http://doi.org/10.1016/j.chempr.2018.12.011.
22. Wang Q, Astruc D. State of the art and prospects in metal-organic framework (MOF)-based and MOF-derived nanocatalysis. Chem Rev. 2020;120(2):1438-511. http://doi.org/10.1021/acs.chemrev.9b00223.
23. Hou CC, Wang HF, Li C, Xu Q. From metal-organic frameworks to single/dual-atom and cluster metal catalysts for energy applications. Energy Environ Sci. 2020;13(6):1658-93. http://doi.org/10.1039/C9EE04040D.
24. Jiao L, Seow JYR, Skinner WS, Wang ZU, Jiang HL. Metal-organic frameworks: structures and functional applications. Mater Today. 2019;27:43-68. http://doi.org/10.1016/j.mattod.2018.10.038.
25. Han L, Qi H, Zhang D, Ye G, Zhou W, Hou C, et al. A facile and green synthesis of MIL-100(Fe) with high-yield and its catalytic performance. New J Chem. 2017;41(22):13504-9. http://doi.org/10.1039/C7NJ02975F.
26. Wang H, Rassu P, Wang X, Li H, Wang X, Wang X, et al. An iron-containing metal–organic framework as a highly efficient catalyst for ozone decomposition. Angew Chem Int Ed. 2018;57(50):16416-20. http://doi.org/10.1002/anie.201810268.
27. Nivetha R, Gothandapani K, Raghavan V, Jacob G, Sellappan R, Bhardwaj P, et al. Highly porous MIL-100(Fe) for the hydrogen evolution reaction (HER) in acidic and basic media. ACS Omega. 2020;5(30):18941-9. http://doi.org/10.1021/acsomega.0c02171.
28. Amouzesh SP, Zandjou M, Ali Khodadadi A, Mortazavi Y, Saboor FH, Saris S, et al. Innovative photocatalyst design: advancing ZnO/MIL-100(Fe) through atomic layer deposition in

hydrogen evolution. ChemCatChem. 2024;16(21):e202401016. http://doi.org/10.1002/cctc.202401016.
29. Barros BS, Lima OJ No, Frós ACO, Kulesza J. Metal-organic framework nanocrystals. ChemistrySelect. 2018;3(26):7459-71. http://doi.org/10.1002/slct.201801423.
30. Zanchetta C, Patton B, Guella G, Miotello A. An integrated apparatus for production and measurement of molecular hydrogen. Meas Sci Technol. 2007;18(5):N21-6. http://doi.org/10.1088/0957-0233/18/5/N02.
31. Saka C, Kaya M, Bekiroğullari M. Spirulina Platensis microalgae strain modified with phosphoric acid as a novel support material for Co–B catalysts: its application to hydrogen production. Int J Hydrogen Energy. 2020;45(4):2872-83. http://doi.org/10.1016/j.ijhydene.2019.11.199.
32. Lestari WW, Meilani R, Nurcahyo I, Larasati L. In situ green synthesis of MIL-100(Fe) modified Edta as an enhanced candidate detoxifying agent of lead heavy metal (Pb) and its adsorption characteristics. Research Square. 2021. http://doi.org/10.21203/rs.3.rs-810297/v1.
33. Deacon GB, Phillips RJ. Relationships between the carbon-oxygen stretching frequencies of carboxylato complexes and the type of carboxylate coordination. Coord Chem Rev. 1980;33(3):227-50. http://doi.org/10.1016/S0010-8545(00)80455-5.
34. Barjasteh M, Vossoughi M, Bagherzadeh M, Pooshang Bagheri K. Green synthesis of PEG-coated MIL-100(Fe) for controlled release of dacarbazine and its anticancer potential against human melanoma cells. Int J Pharm. 2022;618:121647. http://doi.org/10.1016/j.ijpharm.2022.121647.
35. Fang Y, Yang Z, Li H, Liu X. MIL-100(Fe) and its derivatives: from synthesis to application for wastewater decontamination. Environ Sci Pollut Res Int. 2020;27(5):4703-24. http://doi.org/10.1007/s11356-019-07318-w.
36. Wang Z, Miao R, He L, Guan Q, Shi Y. Green synthesis of MIL-100(Fe) derivatives and revealing their structure-activity relationship for 2,4-dichlorophenol photodegradation. Chemosphere. 2022;291(P3):132950. http://doi.org/10.1016/j.chemosphere.2021.132950.
37. Horcajada P, Surblé S, Serre C, Hong DY, Seo YK, Chang JS, et al. Synthesis and catalytic properties of MIL-100(Fe), an iron(III) carboxylate with large pores. Chem Commun. 2007;100(27):2820-2. http://doi.org/10.1039/B704325B.
38. Gong Q, Liu Y, Dang Z. Core-shell structured Fe_3O_4@GO@MIL-100(Fe) magnetic nanoparticles as heterogeneous photo-Fenton catalyst for 2,4-dichlorophenol degradation under visible light. J Hazard Mater. 2019;371:677-86. http://doi.org/10.1016/j.jhazmat.2019.03.019.
39. He Y, Dong W, Li X, Wang D, Yang Q, Deng P, et al. Modified MIL-100(Fe) for enhanced photocatalytic degradation of tetracycline under visible-light irradiation. J Colloid Interface Sci. 2020;574:364-76. http://doi.org/10.1016/j.jcis.2020.04.075.
40. Ozer D, Icten O, Altuntas-Oztas N, Zumreoglu-Karan B. MIL-100(Fe) metal-organic framework catalyzed oxidation of phenol revisited: dark-Fenton activity of the catalyst. Res Chem Intermed. 2020;46(1):909-22. http://doi.org/10.1007/s11164-019-03997-9.
41. Wang J, Imaz I, Maspoch D. Metal-organic frameworks: why make them small? Small Struct. 2022;3(1):2270002. http://doi.org/10.1002/sstr.202270002.
42. Kiren B, Ayas N. Nickel modified dolomite in the hydrogen generation from sodium borohydride hydrolysis. Int J Hydrogen Energy. 2022;47(45):19702-17. http://doi.org/10.1016/j.ijhydene.2021.11.159.
43. Shih YJ, Su CC, Huang YH, Lu MC. SiO_2-supported ferromagnetic catalysts for hydrogen generation from alkaline $NaBH_4$ (sodium borohydride) solution. Energy. 2013;54:263-70. http://doi.org/10.1016/j.energy.2013.01.063.
44. Prasad D, Patil KN, Sandhya N, Chaitra CR, Bhanushali JT, Samal AK, et al. Highly efficient hydrogen production by hydrolysis of $NaBH_4$ using eminently competent recyclable Fe_2O_3 decorated oxidized MWCNTs robust catalyst. Appl Surf Sci. 2019;489:538-51. http://doi.org/10.1016/j.apsusc.2019.06.041.
45. Wang Y, Zhang D, Wang X, Zhang K, Cao Z, Qi N, et al. Co–Fe–B as an effective catalyst for hydrogen production from NaBH4 hydrolysis. Mater Lett X. 2021;12:100104. http://doi.org/10.1016/j.mlblux.2021.100104.
46. Liang Y, Wang P, Dai HB. Hydrogen bubbles dynamic template preparation of a porous Fe-Co-B/Ni foam catalyst for hydrogen generation from hydrolysis of alkaline sodium borohydride solution. J Alloys Compd. 2010;491(1–2):359-65. http://doi.org/10.1016/j.jallcom.2009.10.183.
47. Paksoy A, Kurtoğlu-Öztulum SF, Yağcı MB, Balcı-Çağıran Ö. Low-cost and reusable iron- and nickel-based metal boride nanoparticles for efficient catalytic hydrolysis of sodium borohydride. Int J Hydrogen Energy. 2022;47(87):36898-913. http://doi.org/10.1016/j.ijhydene.2022.08.269.
48. Bariş M, Şimşek T, Taşkaya H. Synthesis of Fe-Fe_2B catalysts via solvothermal route for hydrogen generation by hydrolysis of $NaBH_4$. J Boron. 2018;3(1):51-62. http://doi.org/10.30728/boron.348291.
49. Tian H, Peng J, Du Q, Hui X, He H. One-pot sustainable synthesis of magnetic MIL-100(Fe) with novel Fe_3O_4 morphology and its application in heterogeneous degradation. Dalton Trans. 2018;47(10):3417-24. http://doi.org/10.1039/C7DT04819J.
50. Demirci UB, Miele P. Reaction mechanisms of the hydrolysis of sodium borohydride: a discussion focusing on cobalt-based catalysts. C R Chim. 2014;17(7-8):707-16. http://doi.org/10.1016/j.crci.2014.01.012.
51. Ekinci A. Positive roles of microwave irradiation in hydrogen production from hydrolysis of sodium borohydride using iron oxide catalyst synthesized with watermelon seed peel extract by green method. Int J Hydrogen Energy. 2023;48(76):29615-28. http://doi.org/10.1016/j.ijhydene.2023.04.166.

Data Availability

Data will be made available on request.